Potential Analysis of Iron Nitride Magnets in (Hybrid) Variable Flux Machines

Julius Kesten*, Matthias Brodatzki*, Martin Doppelbauer*
*Institute of Electrical Engineering (ETI), Karlsruhe Institute of Technology, Karlsruhe, Germany
email: julius.kesten@kit.edu

***Abstract*—The novel magnetic alloy iron nitride is investigated both theoretically and with regard to its applicability in (hybrid) variable flux machines ((H)VFM). A review on these machine topologies is given, to contextualize the presented work. An approach to calculate current dependent demagnetization and re-magnetization maps with reduced computational effort is presented. The underlying algorithm uses the data stored per mesh node. A layer topology machine is used to compare the novel magnet material to conventional VFM and also investigate its use in HVFM. Three machines with similar performance are compared with regard to their ability to de- and remagnetize during operation.**

The presented de- and remag map calculation approach works for both VFM and HVFM and reduces the time required for the maps' generation. The novel magnet material iron nitride gives a promising outlook for rare earth free drive systems.

***Index Terms*—hybrid variable flux machine, iron nitride, re-magnetization**

I. Introduction/Structure

Today, most traction systems rely on rare earth enabled permanent magnet synchronous machines (PMSM) to generate propulsion. However, rare earth materials are expensive, are only recycled in small portions and pose a risk in supply chains [1]. To mitigate these risks, alternate machine topologies are investigated, such as (hybrid) variable flux machines (H)VFM. The conventional variable flux machines employ AlNiCo or ferrite alloys. Owing to their low coercive forces, these magnets can be de- and re-magnetized during machine operation by applying adequate stator current pulses.

Thus, the machines operate with regular multiphase stators and require no additional parts in the rotor [2], [3]. For these machines, a magnetization state (Ψ_{rel}) is introduced, representing the permanent magnet (PM) flux linkage $\Psi_{\mathrm{PM,mom}}$ related to the maximum PM flux linkage $\Psi_{\mathrm{PM,max}}$ at full magnetization as in

$$\Psi_{\mathrm{rel}} = \frac{\Psi_{\mathrm{PM,mom}}}{\Psi_{\mathrm{PM,max}}} \cdot 100\,\%. \tag{1}$$

The process of changing Ψ_{rel} is represented in Fig. 2b for a demagnetizing current pulse. The d-axis current is changed to the desired level and then returned back to 0. The d-axis flux linkage is reduced from its initial value and returns to a lower level than before after the current is reduced to 0.

This work was in part financed through the Ministry of Science, Research, and Arts of the Federal State of Baden-Württemberg, Germany, in the framework of "Innovationscampus Mobilität der Zukunft"

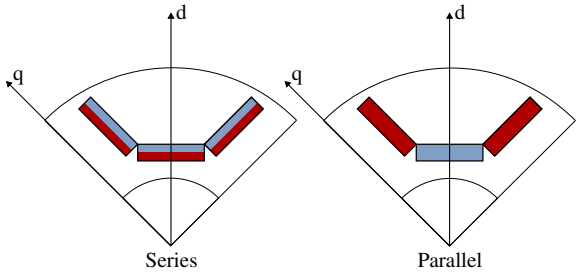

Fig. 1: Series (left) and parallel (right) topologies in HVFM, the magnets are magnetized perpendicularly to their width, blue LCF, red HCF.

In the hybrid configuration, there are both a set of high coercive force (HCF) and low coercive force (LCF) magnets, either arranged in series or parallel. The orientation of the respective magnets is schematically represented in Fig. 1.

While the advantage of parallel structures is a greater range of adjustable magnetization, series topologies have more stable working points of the LCF magnets and further enable easier re-magnetization [4]. The HCF magnets are typically comprised of NdFeB alloys, while the LCF magnets are AlNiCo or Ferrite ones [5]. To make use of both topologies, combinations of parallel and series machines were proposed [6], [7].

Recently, the novel permanent magnetic alloys based on iron nitride (FeN) were introduced and investigations into their application for electric machines were carried out for conventional PMSM. This material appears to have large remanence with coercive forces comparable to those of high-performance ferrite magnets [8], [9]. One of the main reasons FeN is not widely used in industrial applications appears to be mechanical stability: The magnetic properties cited are achieved in nano films rather than magnet blocks [10]. The BH data of FeN magnets presented in this work is based on the BH curve presented in [9].

The performance of (H)VFM is in part determined and limited by the LCF magnets. The maximum operating current under full magnetization is determined by motor topology, as it is directly responsible for the external fields acting on the magnets. It is therefore useful to define an expected operating current in the design process and make the magnets' working point part of the optimization process [11]. While the LCF magnets should have a constant working point during

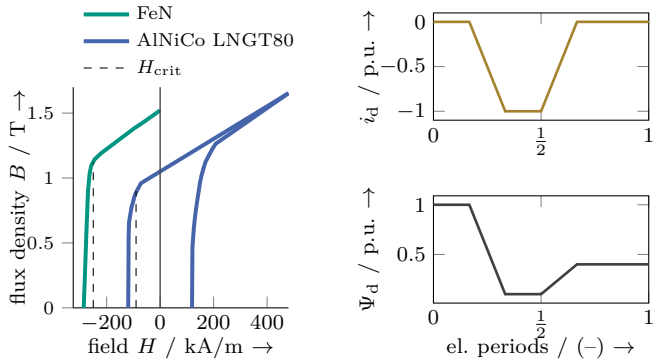

(a) BH curves for the magnet alloys used in this work [9], [13], [14], critical field strengths for "permanent" demagnetization.

(b) Idealized d-current ramp and corresponding flux linkage transient during demagnetization procedure.

Fig. 2: Representation of the BH data used in this work and the process of demagnetization for d-current and flux.

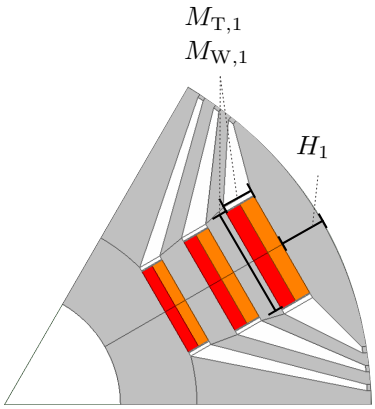

Fig. 3: Parametrized layer rotor topology used in the paper.

normal operation, the ability to change their magnetization is important for inverter design as it determines the maximum required currents. These magnetization characteristics can be represented in current dependent magnetization maps as presented in [12], where the required d-q-current combination to magnetize or demagnetize the magnets to a certain working point is represented. This approach reduces the simulation effort when analyzing control schemes for (H)VFM, since the resulting maps provide look up tables in the control scheme, making magnetization caluclations obsolete in control simulation setups. The authors of [12] further use the novel FeN alloy in the VFM reported on. However, the application presented is a conventional VFM, not a hybrid one.

The aim of this work is to investigate the novel FeN magnets and their applicability in HVFM. The FeN magnets are compared directly to AlNiCo in conventional VFM as a base line. Further, the FeN magnets are used as HCF and the AlNiCo as LCF magnets in a series configuration HVFM.

The BH data of all magnets used is represented in Fig. 2a. The re-magnetizing behavior of the AlNiCo is represented, because it needs to be known for the re-magnetiziation process in the HVFM, and because there is no re-magnetizing data available for FeN magnets to the knowledge of the authors.

A workflow to calculate the re-magnetization maps of a machine based on the relation between its magnets' BH curve and the current dependent demag map is presented. The new tool is then used to carry out the performance comparison mentioned above. The paper is structured as follows: In section II the data common to all investigated machines is presented and the re-mag map calculation workflow is introduced. Section III gives an overview of the simulations carried out and introduces the design of experiment used in the investigation. In the subsequent section IV the three different machines are compared with regard to their performance and their magnetizing behavior. Finally, in section V the work is summarized and an outlook on future research is given.

II. Machine Model and Magnetization Map Computation

The machine model in this work is a layer geometry, yielding a large portion of reluctance torque. Its main features will be presented in the subsection below.

As explained above, the calculation of demag and re-mag maps is advantageous for the investigation of (H)VFM. Since further information on the magnets' operating points in the machine may be of interest and to reduce the computational effort required for the re-mag map generation, an approach relying on the vector potential $\vec{A}$ in each mesh node is introduced. The post processing of the mesh data is carried out based on the considerations presented in [15].

A. Machine Model

The parametrized layer rotor topology used in this investigation is presented in Fig. 3. The magnets are divided perpendicularly to their direction of magnetization for the HVFM analysis. The HCF magnets are marked in red in the figure. For the VFM calculations the magnets are left undivided. For either magnet the width $M_{\mathrm{W},i}$ and the thickness $M_{\mathrm{T},i}$ are parametrized. In addition to the magnets' dimensions, their radial position in the rotor is defined by the parameters H_i. To enable the HVFM analyses, the magnet ratio $M_{\mathrm{R},i}$ is introduced for each magnet individually:

$$M_{\mathrm{R},i} = \frac{M_{\mathrm{T,HCF}}}{M_{\mathrm{T},i}} \tag{2}$$

It represents the share of the HCF magnet in either magnet's thickness. Note, that the parameters for magnet 2 and magnet 3 are not represented in Fig. 3 to enhance readability. They are nonetheless considered in the following considerations.

In series HVFM with different B_{rem} in the LCF and HCF magnets the interface condition

$$(\vec{B}_1 - \vec{B}_2) \cdot \vec{n}_{12} = 0 \tag{3}$$

between both magnets must be considered, where B_{i} represents the flux density vector on either side of the interface and $\vec{n}_{12}$ represents the normal unit vector of the interface. Thus, if the difference in B_{rem} between both magnet materials

is large, one magnet will magnetize the other. This can even lead to involuntary demagnetization of the HCF magnets even under no-load conditions.

The investigated machine's base data is presented in Tab. I. The dataset given in the table is left unaltered in the design of experiment (DoE) described in section III

TABLE I: Common properties of the simulated machines.

Property	Value	Unit
Outer diameter D_o	120	mm
Bore diameter D_b	80	mm
Air gap length δ	0.5	mm
Length l_fe	80	mm
No. of slots N_s	36	-
No. of pole pairs p	3	-
No. of conductors per coil Z_c	10	-
Parallel branches a	1	-
Rated current I_rms	45	A
DC link voltage V_dc	400	V
Max. speed n_max	15000	$1/\mathrm{min}$

B. Remagnetization Calculation

To fully describe VFM, their behavior when subjected to both demagnetizing and re-magnetizing currents is of relevance. Typically both a demagnetization and a magnetization ramp need to be simulated consecutively to generate demag and remag maps as described in [12]: Initially, a demagnetizing current pulse is imposed on the machine and the resulting Ψ_rel is recorded. Consequently, and in the same FEA simulation, a re-magnetizing current pulse is imposed to enhance the Ψ_rel and the new, re-magnetized Ψ_rel is recorded. The resulting maps represent the respective Ψ_rel in dependence of i_d and i_q, i.e. the remaining PM flux after returning the current to 0.

To calculate the re-magnetization maps, two electrical periods need to be simulated to achieve the desired result (one period for demag maps). This is time consuming compared to the typical 1/6 period used for simulations of electrical machines. Further, the utilized FEA needs to be able to calculate remagnetization of permanent magnets, which is not given for all solvers, unlike demagnetization.

Both problems can be mitigated by combining the system characteristics of the electric machine and the material characteristics of the permanent magnets with the knowledge of the magnets' inherent properties, i.e. their recoil behavior. An overview of the presented process is given in Fig. 4. In the figure, input data to the process is represented in blue trapezoidal nodes, process/simulation steps are represented in gray rectangular nodes and result data is given as beige trapezoidal nodes. The arrows denoted with "Mesh PP" represent processes, which directly access the vector potential $\vec{A}$ stored per mesh node and use the post processor described in [15] to calculate the flux density $\vec{B}$ and field strength $\vec{H}$ per mesh element.

Firstly, a demagnetization calculation is carried out for different dq combinations with negative (i.e. demagnetizing) d-currents to generate a demag map (node "Demag simulation"),

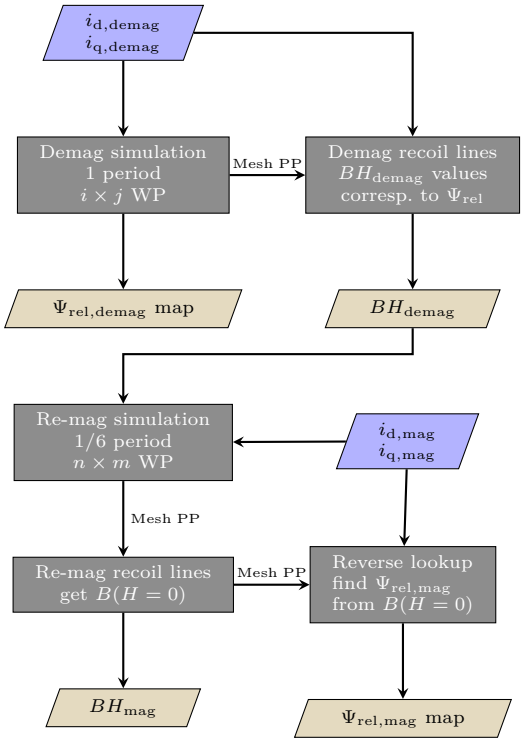

Fig. 4: Re-magnetization calculation workflow with blue boxes denoting external input parameters, gray boxes denoting calculation steps and beige boxes denoting resulting data.

see Fig. 2b. A full electrical period is analyzed. Additionally, the mesh in each permanent magnet is exported and the flux density B and field strength H are calculated based on the vector potential A for each mesh element (node "Demag recoil lines"). To do so, the BH-curve in the second quadrant must be provided.

Hereupon a cumulative BH working point as the mean over all magnets is calculated. Using the magnets' recoil permeability for demagnetization processes their working point for $H = 0$ is calculated using the flux densities and field strengths calculated for the maximum magnitude of the demagnetizing current pulse (i.e. the value of i_d between 2/6 and 1/2 of the electrical period in Fig. 2b, see node "Demag recoil lines"). After this calculation step, the BH working points under load and for $H = 0$ have been calculated, as well as the Ψ_rel after demagnetization. Both datasets are stored as current dependent maps.

Subsequently, a second FEA simulation is carried out, now calculating the machine behavior for dq current combinations with positive (i.e. re-magnetizing) d-currents. The current values may differ both in magnitude and number from those provided for the demagnetization calculations. The simulation covers 1/6 of an electrical period during which the dq current values are kept constant (node "Re-mag simulation"). The first quadrant of the magnets' BH-curve must be provided to generate the correct results, as represented in the right half-plane of Fig. 2a. The BH data under load is calculated.

With the knowledge of the magnets' recoil permeability, the working point for $H = 0$ is calculated, yielding current dependent recoil lines ("Re-mag recoil lines").

To accord the previously calculated demagnetization Ψ_{rel} – a machine characteristic – with the re-magnetization BH operating points, which represent a material characteristic, recoil values $B_{\mathrm{mag}}|_{H=0} = B_{\mathrm{demag}}|_{H=0}$ are sought. Due to the discretization of the results in the $\vec{i}_{\mathrm{dq,demag}}$ and $\vec{i}_{\mathrm{dq,mag}}$ plane respectively, this pairing imposes an optimization problem (node "Reverse lookup"). The corresponding flux density for a specific dq current pair in the re-magnetizing plane is defined as B_{search}. An optimization function can be defined as:

$$f_{\mathrm{opt}}(\vec{i}_{\mathrm{dq,fit}}) = \left| B_{\mathrm{search}} - B_{\mathrm{demag}}|_{H=0} \left(\vec{i}_{\mathrm{dq,fit}}\right) \right| \quad (4)$$

$$\min \left(f_{\mathrm{opt}}(\vec{i}_{\mathrm{dq,fit}}) \right) \quad (5)$$

Where $\vec{i}_{\mathrm{dq,fit}}$ represents the dq currents from the demagnetizing calculations. The current pair that solves (4) for zero is used in the previously calculated $\Psi_{\mathrm{rel,demag}}$ lookup table ("$\Psi_{\mathrm{rel,demag}}$ map"). This Ψ_{rel} is the re-magnetizing $\Psi_{\mathrm{rel,mag}}$ sought after for the initially defined re-magnetizing dq pair, corresponding to B_{search}.

The principle is represented in Fig. 5, where the dashed line represents the magnets' behavior for re-magnetizing operations and the dotted line represents the corresponding demagnetizing process. Since both lines meet for $H = 0$, they represent the same Ψ_{rel}. Therefore, if B_{search} is accorded with the equal B_{demag}, the corresponding re-magnetizing Ψ_{rel} is found via the corresponding current pair.

This approach is time saving compared to the conventional approach for re-mag map calculation, because only 1/6 electrical period needs be simulated for the re-magnetizing part. The amount of time required for demagnetization remains the same. However, 5/6 less simulation time is required on the re-mag side, resulting in a total simulation requirement of 7/6 electrical periods with this approach compared to 12/6 with the conventional one. It implicitly works for both conventional VFM and HVFM: Only the LCF is considered in the case of an HVFM. Its operating points are affected by the HCF magnet in the same way for demagnetized and a re-magnetized Ψ_{rel}. The field of the HCF acts as a magnetizing agent, thus resulting in an offset of the LCF operating point, both for de- and remagnetization. Therefore, the approach is also applicable for HVFM.

The proposed approach is validated by calculating the demagnetizing Ψ_{rel}. Data points are removed from an $\Psi_{\mathrm{rel,demag}}$ map and the corresponding values $B_{\mathrm{demag}}|_{H=0}$ are used to calculate the missing Ψ_{rel} point. This is carried out for an entire current dependent demag map of a machine, and the relative error is calculated as

$$E = \frac{y_i - y_0}{y_0} \quad (6)$$

where y_i are the estimated magnetization states and y_0 are those calculated via FEA. An average error of 3-7.2 % was achieved, depending on the machine topology and the resolution of the simulated current grid. Thus, the method is deemed suitable for the suggested purpose.

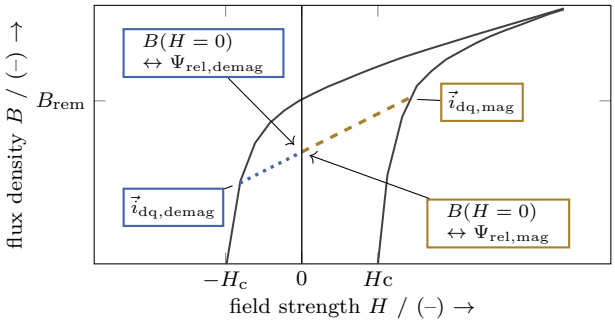

Fig. 5: Schematic representation of the accordance between re-magnetizing and demagnetizing dq-current pairs with regard to the BH curve and the recoil lines.

III. Simulation

The FEA simulations presented in this work are carried out using Ansys Electronics. The magnets are modeled using the BH curves presented in Fig. 2a. Three machine types are considered: A layer type with AlNiCo LNGT80 magnets only, a layer type with FeN magnets only, and a layer type with a series hybrid configuration with AlNiCo and FeN magnets, where the FeN magnets are the HCF ones, see Fig. 3.

A design of experiment (DoE) of 500 machines each was carried out using latin hypercube sampling for the single magnet machines. In the hybrid machine, the DoE size was 750 machines to take into account the magnet ratio $M_{\mathrm{R},i}$ as additional parameter. The varied parameters' minimum and maximum values are listed in Tab. II. For paramters, whose range is equal for all magnets, the subscript i is used.

TABLE II: Variation parameters in the DoE investigated.

Parameter	Range	Unit
$M_{\mathrm{T},i}$	2 - 4	mm
$M_{\mathrm{W},1}$	6 – 15	mm
$M_{\mathrm{W},2}$	7 – 15	mm
$M_{\mathrm{W},3}$	8 – 15	mm
H_1	3 – 7	mm
H_2	9 – 12	mm
H_3	14 – 20	mm
$M_{\mathrm{R},i}$	0.2 – 0.8	-

The magnetization maps (i.e. demag and re-mag maps) for the AlNiCo and the hybrid machine were calculated. For the FeN machine, only a demag map is presented, because no re-magnetization data could be provided.

For the results discussion, one machine out of each dataset was selected with a maximum output torque $T_{\mathrm{max}} = T_{\mathrm{sh}} = 27\,\mathrm{N\,m}$. These machines represent a middle ground out of the results of each dataset.

IV. Results

The performance data of the selected machines is presented in Fig. 6. The mechanical shaft torque T_{sh} and power P_{sh} are

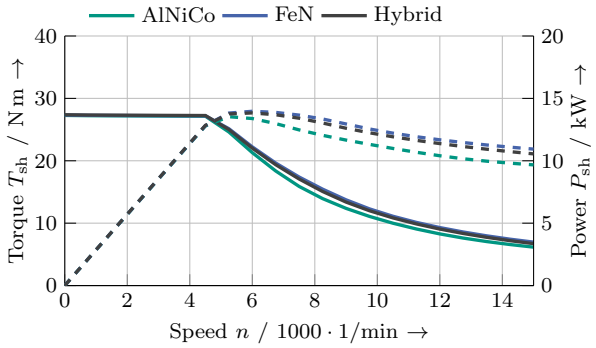

Fig. 6: Torque-speed envelopes of the machines under investigation, torque in solid lines, power in dashed lines.

presented as the torque-speed envelope. All three machines have a similar corner point at $n_{\mathrm{corner}} \approx 4500\,1/\mathrm{min}$. The AlNiCO machine's maximum power is $13.5\,\mathrm{kW}$. For the FeN machine it is $14.0\,\mathrm{kW}$ and $13.8\,\mathrm{kW}$ for the hybrid one. In the field weakening range, the FeN and hybrid machine consequently exceed the AlNiCo machine's power. The FeN machine has the largest power. Table III shows the key data

TABLE III: Key data of the presented result machines.

	AlNiCo	FeN	Hybrid
Maximum power (kW)	13.5	14.0	13.8
Maximum torque (N m)	27.27	27.33	27.38
Total magnet area (%)	100	74.6	87.8
Relative HCF area (%)	–	–	33.1

of all three machines. The total magnet area is normalized to the AlNiCo machine. The relative HCF area represents the portion of HCF magnets of the total magnet area of the hybrid machine. The FeN machine requires the least amount of magnetic material, which is to be expected due to the material's superior characteristics compared to the AlNiCo alloy.

The overall performance of all three sample machines is similar. Therefore, they are deemed suitable for the comparison of their magnetizing characteristics.

For each machine, the demag and re-mag (save for the FeN machine) maps are presented in Fig. 7. The x-axis of the figures represents the current angle ϑ, which is the angle between the q-axis and the current phasor, i.e. $\vartheta = 0$ represents pure q-current (see Fig.7f). Note that for the re-magnetizing data, negative angles occur, since positive d-currents are required for this operation. The y-axis represents the rms value of the stator current applied. For the demag maps the maximum current magnitude is $I_{\mathrm{demag,max}} = 4 \cdot I_{\mathrm{rms,nom}} = 180\,\mathrm{A}$, for the re-mag maps it is $I_{\mathrm{mag,max}} = 8 \cdot I_{\mathrm{rms,nom}} = 360\,\mathrm{A}$.

In comparison between the AlNiCo and the hybrid machine, the advantages of hybridization discussed in section I can be recognized. While the AlNiCo machine demagnetizes more easily and reaches a minimum Ψ_{rel} at a current magtnitude of $45\,\mathrm{A}$, i.e approximately at nominal current, the hybrid machine holds a residual magnetization up to almost $180\,\mathrm{A}$. The re-mag maps illustrate the positive effect of hybridization in VFM of reducing the re-magnetizing current magnitudes. While the AlNiCo machine does not reach a maximum Ψ_{rel} above $75\,\%$, this value can be reached with a current magnitude of approx. $150\,\mathrm{A}$ in the hybrid machine.

The demagnetization map of the FeN machine shows the effect of the larger coercivity of the FeN alloy compared to AlNiCo. Its minimum Ψ_{rel} in demagnetization is above $50\,\%$ and considerably higher than the AlNiCo and the hybrid machines'. This is partly due to the effect described in section II, where the FeN magnet as the HCF is "pre-loaded" by the LCF AlNiCo. Further, the total thickness of the FeN magnets used in the hybrid topology is smaller than for the "pure" FeN machine, since the overall thickness of the magnets is kept the same for the non-hybrid and hybrid machines (see Tab. III). Since the thickness of a magnet is relevant to its withstanding of demagnetizing field, this appears to be conclusive.

Overall, the application of FeN magnets in the machines discussed above leads to a reduction in magnet material requirements for a given performance, or an improved output torque and power for a given magnet volume.

V. Conclusion and Outlook

The novel magnet alloy iron nitride was introduced and its limitiations, due to availability and mechanical sturdiness, were presented. An approach to calculate re-mag maps for (H)VFM was presented. It takes advantage of the connection between the machine's current dependent Ψ_{rel} during demagnetization calculations and the operating points on the magnets' BH curves during re-magnetization. The presented approach reduces the time required for re-mag map calculation while maintaining good accuracy.

A layer topology (H)VFM was investigated with three different magnet setups. The proposed method for magnetization map calculation was applied and the magnetizing properties of the different machines were compared. The iron nitride enabled HVFM has improved persistence towards demagnetizing currents. It presents with better re-magnetizating behavior than the non-hybrid AlNiCo VFM. The investigated FeN machine has a better capability to withstand demagnetizing than that of both the AlNiCo VFM and the HVFM. This is due to demagnetization of the FeN magnets in the hybrid machine, where they partly magnetize the AlNiCo magnets to satisfy the interface condition in multi material magnetic systems. In comparison to the widely-used neodymium magnets, the performance of the machines presented in this work is small. The much larger coercive field of the rare earth magnet, however, hinders demagnetization more than the FeN magnet does, thus reducing the beneficial effects of (H)VFM in high speed operation.

To further improve result quality of the magnetization maps, a sample of an AlNiCo magnet will be measured to acquire reliable data for both its demagnetizing and re-magnetizing behavior. The future development of FeN magnets will be

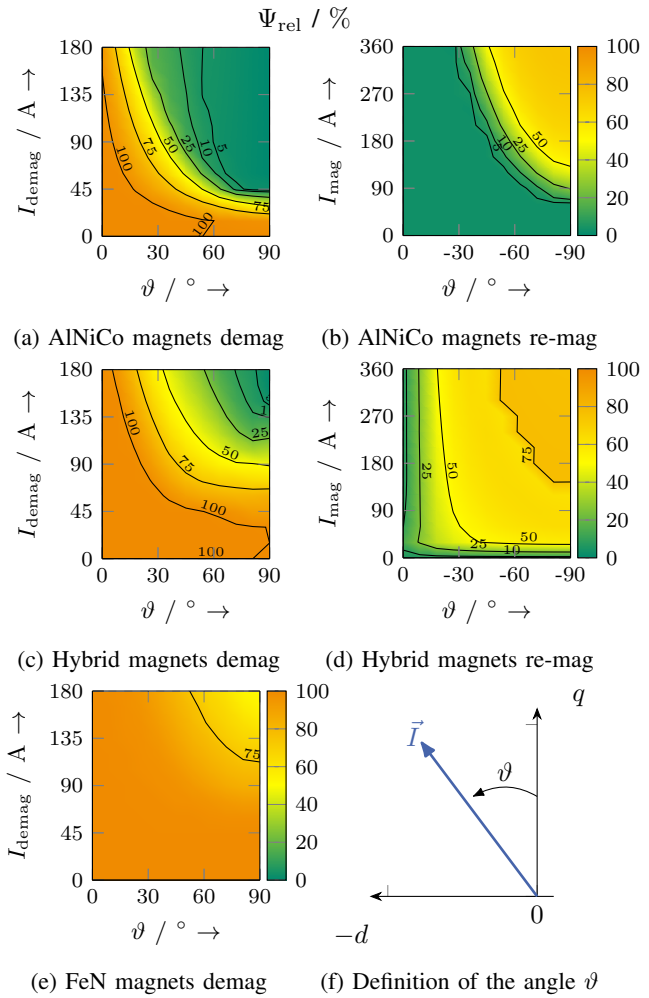

Fig. 7: Demagnetization and re-magnetization maps for the selected layer machines with $T_{\max} \approx 27\,\mathrm{N\,m}$, definition of current angle ϑ.

observed. Once samples become available, measurement data will also be used to allow re-magnetization calculations for FeN-enabled machines. In the investigations carried out in this work, the material gives a promising outlook for rare earth free drive systems.

Future investigations into the machine design presented in this work will include a multi objective optimization as a means to find a balance between the required Ψ_{rel} for optimum efficiency and the de- and re-magnetizing capabilities. This allows an informed inverter selection and therefore offers a perspective for overall drive train efficiency optimization.

References

[1] European Commission. Directorate General for Internal Market, Industry, Entrepreneurship and SMEs., *Study on the critical raw materials for the EU 2023: final report.* LU: Publications Office, 2023. [Online]. Available: https://data.europa.eu/doi/10.2873/725585

[2] V. Ostovic, "Memory motors," *IEEE Industry Applications Magazine*, vol. 9, no. 1, pp. 52–61, Jan. 2003.

[3] K. Sakai, K. Yuki, Y. Hashiba, N. Takahashi, and K. Yasui, "Principle of the variable-magnetic-force memory motor," in *2009 International Conference on Electrical Machines and Systems*. IEEE, 2009, pp. 1–6.

[4] H. Yang, S. Lyu, H. Lin, Z.-q. Zhu, H. Zheng, and T. Wang, "A Novel Hybrid-Magnetic-Circuit Variable Flux Memory Machine," *IEEE Transactions on Industrial Electronics*, vol. 67, no. 7, pp. 5258–5268, Jul. 2020. [Online]. Available: https://ieeexplore.ieee.org/document/8786909/

[5] M. Ibrahim and P. Pillay, "Design of Hybrid Variable Flux Motors for Enhanced Wide-Speed Performance," in *2019 IEEE Energy Conversion Congress and Exposition (ECCE)*. IEEE, Sep. 2019, pp. 6046–6053.

[6] X. Zhao, H. Lin, Y. Zhong, W. Liu, and H. Yang, "A Novel Separated Hybrid-Magnetic-Circuit Variable Flux Memory Machine," *IEEE Transactions on Industrial Electronics*, vol. 70, no. 12, pp. 12 060–12 070, Dec. 2023. [Online]. Available: https://ieeexplore.ieee.org/document/10018894/

[7] W. Liu, H. Yang, H. Lin, S. Lyu, and Y. Zhong, "A Novel Variable Flux Memory Machine With Separated Series–Parallel PM Structure," *IEEE Transactions on Industrial Electronics*, vol. 70, no. 4, pp. 3348–3361, Apr. 2023, publisher: Institute of Electrical and Electronics Engineers (IEEE). [Online]. Available: https://ieeexplore.ieee.org/document/9778961/

[8] R. Wilson, P. Kumar, A. Al-Qarni, Q. Ma, and A. El-Refaie, "Robustness of Dynamic FEA-based Demagnetization Calculation in the Multi-Objective Optimization of PM-assisted Synchronous Reluctance Motor with Blended Magnets," in *2023 IEEE International Electric Machines & Drives Conference (IEMDC)*. San Francisco, CA, USA: IEEE, May 2023, pp. 1–7. [Online]. Available: https://ieeexplore.ieee.org/document/10239082/

[9] R. Wilson, P. Kumar, and A. El-Refaie, "Comparative Analysis and Optimization of Iron Nitride Enabled 800-V PM-Assisted Synchronous Reluctance Traction Motor with Varying Poles for Extended Operating Speed Range," in *2024 International Conference on Electrical Machines (ICEM)*. Torino, Italy: IEEE, Sep. 2024, pp. 1–7. [Online]. Available: https://ieeexplore.ieee.org/document/10700537/

[10] I. Dirba, M. Mohammadi, F. Rhein, Q. Gong, M. Yi, B.-X. Xu, M. Krispin, and O. Gutfleisch, "Synthesis and magnetic properties of bulk α''-Fe16N2/SrAl2Fe10O19 composite magnets," *Journal of Magnetism and Magnetic Materials*, vol. 518, p. 167414, Jan. 2021. [Online]. Available: https://linkinghub.elsevier.com/retrieve/pii/S0304885320323817

[11] J. Kesten, F. Frölich, F. Wittemann, J. Knirsch, F. Bechler, L. Kärger, P. Eberhard, F. Henning, and M. Doppelbauer, "Design Approach for a Novel Multi Material Variable Flux Synchronous Reluctance Machine without Rare Earth Magnets," in *2022 International Conference on Electrical Machines (ICEM)*. IEEE, 2022, pp. 2304–2310.

[12] M. S. Mirazimi, C. Chen, P. Pescetto, S. Ferrari, G. Pellegrino, M. Diana, and T. Thiringer, "Accurate Modeling of Variable- Flux PMSMs without Electromagnetic Co-Simulation," in *2024 International Symposium on Power Electronics, Electrical Drives, Automation and Motion (SPEEDAM)*. Napoli, Italy: IEEE, Jun. 2024, pp. 625–630. [Online]. Available: https://ieeexplore.ieee.org/document/10609051/

[13] G. Gallicchio, M. D. Nardo, M. Palmieri, and F. Cupertino, "Analysis, Design and Optimization of Hysteresis Clutches," *IEEE Open Journal of Industry Applications*, vol. 1, pp. 258–269, 2020. [Online]. Available: https://ieeexplore.ieee.org/document/9285185/

[14] A. M. Technologies, "Cast ALNICO Permanent Magnets," Feb. 2003. [Online]. Available: https://www.arnoldmagnetics.com/wp-content/uploads/2017/10/Cast-Alnico-Permanent-Magnet-Brochure-101117.pdf

[15] M. Greule, M. Boxriker, B. Zhang, and M. Doppelbauer, "Numerical iron loss computation method for switched reluctance motors," in *2016 18th European Conference on Power Electronics and Applications (EPE'16 ECCE Europe)*. Karlsruhe: IEEE, Sep. 2016, pp. 1–10. [Online]. Available: http://ieeexplore.ieee.org/document/7695476/

BIOGRAPHIES

Julius Kesten received his M.Sc in Mechatronics and Information Technology 2020 from the Karlsruhe Institute of Technology (KIT), Germany. Since 2020 he works at the Institute of Electrical Engineering at the KIT. His research interests include the design of synchronous reluctance and variable flux machines. He focuses on the design and operation of variable flux machines with regard to optimum efficiency.

Matthias Brodatzki was born in Bytom, Poland in 1988. He received the M.Sc. degree in electrical engineering from the Karlsruhe Institute of Technology (KIT) in 2014. He received his doctorate degree at the Institute of Electrical Engineering (ETI) and is now research group leader with this institute in the field of electrical machines and drives.

Martin Doppelbauer was born in Altenhundem, Germany. He received the Dipl.-Ing. and Dr.-Ing. degrees in electrical engineering from the University of Dortmund, Germany in 1990 and 1995, respectively. He was with the companies Danfoss Bauer in Esslingen and SEW Eurodrive in Bruchsal, Germany, as Senior Manager for electric motor development. Since 2011 he is full professor at the Institute of Electrical Engineering (ETI) at the KIT. He holds a chair for Hybrid Electric Vehicles. Martin Doppelbauer is also active in national and international standardization and the chairman of IEC Technical Committee 2 Rotating Electrical Machines.